



# EGFR targeted nanobody–photosensitizer conjugates for photodynamic therapy in a pre-clinical model of head and neck cancer



Pieter B.A.A. van Driel<sup>a,b,1,2</sup>, Martin C. Boonstra<sup>c,1</sup>, Maxime D. Slooter<sup>a,b,2</sup>, Raimond Heukers<sup>d</sup>, Marieke A. Stammes<sup>a,b,2</sup>, Thomas J.A. Snoeks<sup>a</sup>, Henriette S. de Bruijn<sup>e</sup>, Paul J. van Diest<sup>f</sup>, Alexander L. Vahrmeijer<sup>c</sup>, Paul M.P. van Bergen en Henegouwen<sup>d</sup>, Cornelis J.H. van de Velde<sup>c</sup>, Clemens W.G.M. Löwik<sup>a,2</sup>, Dominic J. Robinson<sup>e</sup>, Sabrina Oliveira<sup>d,\*</sup>

<sup>a</sup> Department of Radiology, Division of Molecular Imaging, Leiden University Medical Center, Albinusdreef 2, 2333 ZA Leiden, The Netherlands

<sup>b</sup> Percuro BV, Drienerlolaan 5, 7522 NB Enschede, The Netherlands

<sup>c</sup> Department of Surgery, Leiden University Medical Center, Albinusdreef 2, 2333 ZA Leiden, The Netherlands

<sup>d</sup> Molecular Oncology, Cell Biology Division, Department of Biology, Faculty of Science, Utrecht University, Padualaan 8, 3584 CH Utrecht, The Netherlands

<sup>e</sup> Department of Otorhinolaryngology & Head and Neck Surgery, Center for Optical Diagnostics and Therapy, Erasmus Medical Center, s-Gravendijkwal 230, 3015 CE Rotterdam, The Netherlands

<sup>f</sup> Department of Pathology, University Medical Center Utrecht, Heidelberglaan 100, 3584 CX Utrecht, The Netherlands

## ARTICLE INFO

### Article history:

Received 16 December 2015

Received in revised form 7 March 2016

Accepted 9 March 2016

Available online 15 March 2016

### Keywords:

Photodynamic therapy

Tumor targeting

Nanobody or VHH

Quantitative fluorescence spectroscopy

EGFR

Head and neck cancer

## ABSTRACT

Photodynamic therapy (PDT) induces cell death through local light activation of a photosensitizer (PS) and has been used to treat head and neck cancers. Yet, common PS lack tumor specificity, which leads to collateral damage to normal tissues. Targeted delivery of PS via antibodies has pre-clinically improved tumor selectivity. However, antibodies have long half-lives and relatively poor tissue penetration, which could limit therapeutic efficacy and lead to long photosensitivity. Here, in this feasibility study, we evaluate at the pre-clinical level a recently introduced format of targeted PDT, which employs nanobodies as targeting agents and a water-soluble PS (IRDye700DX) that is traceable through optical imaging. *In vitro*, the PS solely binds to cells and induces phototoxicity on cells overexpressing the epidermal growth factor receptor (EGFR), when conjugated to the EGFR targeted nanobodies. To investigate whether this new format of targeted PDT is capable of inducing selective tumor cell death *in vivo*, PDT was applied on an orthotopic mouse tumor model with illumination at 1 h post-injection of the nanobody–PS conjugates, as selected from quantitative fluorescence spectroscopy measurements. In parallel, and as a reference, PDT was applied with an antibody–PS conjugate, with illumination performed 24 h post-injection. Importantly, EGFR targeted nanobody–PS conjugates led to extensive tumor necrosis (approx. 90%) and almost no toxicity in healthy tissues, as observed through histology 24 h after PDT. Overall, results show that these EGFR targeted nanobody–PS conjugates are selective and able to induce tumor cell death *in vivo*. Additional studies are now needed to assess the full potential of this approach to improving PDT.

© 2016 The Authors. Published by Elsevier B.V. This is an open access article under the CC BY-NC-ND license (<http://creativecommons.org/licenses/by-nc-nd/4.0/>).

## 1. Introduction

Cancers of the head and neck region are the sixth most common cancers in the world [1]. In spite of recent advances in surgery and radiotherapy, increasing incidences and moderate survival rates are reported [2]. Photodynamic therapy (PDT) is a promising minimally invasive approach that is being used for the local treatment of premalignant and malignant lesions in the head and neck region [3,4]. Despite the

potential advantages of PDT, collateral damage to normal tissue remains a significant side effect, particularly in the treatment of large tumors [5]. Targeted PDT, in which photosensitizers (PS) are selectively delivered to the tumor, could greatly enhance the results of PDT in head and neck cancer.

PDT makes use of three essential elements to induce localized (tumor) cell death: a PS, light of a particular wavelength, and oxygen [3]. Although each of these individual components is not toxic, together they induce local toxicity through the formation of toxic reactive oxygen species, notably singlet oxygen ( $^1\text{O}_2$ ), damaging proteins, lipids and/or nucleic acids. The lifetime and diffusion distance of  $^1\text{O}_2$  are very short [6], consequently, the localization of PS at the time of the illumination is a critical factor in the selectivity of PDT. The overall localization of the PS at the tumor and the surrounding normal tissues is determined by the pharmacokinetics of the PS (i.e. its absorption, distribution,

\* Corresponding author at: Molecular Oncology (Room N510), Division of Cell Biology, Department of Biology, Faculty of Science, Utrecht University, Padualaan 8, 3584 CH Utrecht, The Netherlands.

E-mail address: [s.oliveira@uu.nl](mailto:s.oliveira@uu.nl) (S. Oliveira).

<sup>1</sup> Both authors contributed equally to this work and share first-authorship.

<sup>2</sup> Current address: Department of Radiology, Division of Optical Molecular Imaging, Erasmus Medical Center, s-Gravendijkwal 230, 3015 CE Rotterdam, The Netherlands.

metabolism, and excretion). The generation of  $^1\text{O}_2$  in the target tissue results in cell death through apoptosis and/or necrosis. Necrotic cell death can be induced either by a direct effect on tumor cells or indirectly through a shutdown of tumor vasculature. An important additional mechanism of action in PDT is derived from a robust inflammatory response that can lead to development of systemic immunity [3].

Clinically available PSs can be categorized as derivatives of three major families: porphyrins (e.g. Photofrin), chlorins (e.g. Foscan) and phthalocyanines (e.g. Photosense) [7]. In general, most PSs are rather hydrophobic which promotes cell binding, but provides no specificity. As a result, 2 to 4 days are generally necessary between injection of the PS and illumination, in order to favor clearance of PS from normal tissues and to promote some tumor specificity [7]. Alternatively, light can be applied earlier after PS administration, with the particular intention to induce vascular damage [3]. In addition, patients generally show skin photosensitivity for long periods of time (2–6 weeks) [3,8]. Therefore, efforts have been made to render PS more hydrophilic and to target these molecules more selectively to tumors, through chemical modifications, delivery systems, and/or targeting molecules [9–13]. The targeting of PS through the use of monoclonal antibodies (mAbs), which is termed photoimmunotherapy [11], has shown promising results [14,15]. Nevertheless, due to their large molecular weight (150 kDa), mAb–PS conjugates have a limited capability of penetrating into the interior of large tumors [16,17]. Moreover, the larger size of mAbs–PS conjugates (~15 nm) may impede the generation of  $^1\text{O}_2$  within the outer cell membrane of targeted cells and affect the therapeutic efficacy. The location of lipophilic photosensitisers within the plasma membrane has previously been shown to influence *in vitro* and *in vivo* efficacy [18]. Furthermore, because of long half-lives of mAbs in the bloodstream, time is needed for tumor accumulation and development of sufficient tumor-to-background ratios (TBR) to protect healthy tissues. As many of these disadvantages are related to the size of mAbs, some studies reported the use of smaller mAb fragments such as F(ab')<sub>2</sub> and scFv conjugated to a PS [19–24].

Recently, we have introduced an alternative approach for targeted PDT employing nanobodies conjugated to a water-soluble and traceable PS, leading to encouraging results *in vitro* [25]. Nanobodies are the smallest naturally derived antigen-binding fragments that consist of the variable domain of heavy chain antibodies, which were first discovered in dromedaries in 1993 [26]. Nanobodies bind specifically and with high affinities to their antigens [26,27], they are stable and soluble in aqueous solutions, can be chemically modified, and have low immunogenic potential [28]. Importantly, with a molecular weight ten times smaller than conventional antibodies (15 kDa vs 150 kDa) [29] and high binding affinities, tumor penetration of nanobodies is greatly enhanced, and occurs more rapidly [27,30,31] (this is in line with the modeling of Schmidt and Wittrup [32]). In addition, the rapid clearance through the kidneys accelerates the acquisition of images with sufficient TBR, as demonstrated in our previous studies in which a nanobody was compared to an antibody for optical molecular imaging [30,31]. The nanobodies that we used for PDT, i.e. the monovalent 7D12 [31,33] and the biparatopic 7D12-9G8 [34], specifically targeted the epidermal growth factor receptor (EGFR). With more than 83% of all head and neck squamous cell carcinomas overexpressing EGFR [35], it serves as a promising target in head and neck cancer patients. In fact, increased levels of EGFR are associated with poor prognosis by locoregional failure and decreased survival [36]. The PS that we conjugated to the nanobodies was IRDye700DX, which is a water-soluble silicon-phthalocyanine derivative, that has a strong absorption band in the near-infrared region of the spectrum (690 nm) and is also traceable through optical imaging [15,37]. Our previous studies showed that, *in vitro*, the nanobody–PS conjugates (i.e. 7D12–PS and 7D12-9G8–PS) bound specifically to EGFR, allowing the distinction of cell lines with different expression levels of EGFR. Notably, the conjugates specifically induced cell death of EGFR overexpressing cells in low nanomolar concentrations. Importantly, the biparatopic conjugate (i.e. 7D12-9G8–PS) was more toxic, as it could deliver more PS

intracellularly [25], via the clustering induced endocytosis of EGFR [38]. These encouraging results have stimulated further investigation of these conjugates in an *in vivo* setting.

The aim of the present study is to investigate the therapeutic potential of nanobody–PS conjugates for targeted PDT, i.e. to determine whether these conjugates are capable of inducing selective tumor cell death *in vivo*, in a pre-clinical head and neck tumor model. First, the nanobody–PS conjugates are characterized for their specificity and phototoxicity *in vitro* employing the EGFR overexpressing oral squamous cell carcinoma cell line OSC-19-luc2-cGFP (OSC). Subsequently, this cell line is grown as an orthotopic model in the tongue of mice to allow pre-clinical evaluation through histological analysis post-PDT. As a reference or positive control, and for validation of the model and analysis procedure employed in this feasibility study, Cetuximab–PS was employed as Mitsunaga et al. [15] have described the use of their mAb–PS conjugates. To determine the best time point for illumination after intravenous injection of the nanobody–PS conjugates, quantitative fluorescence spectroscopy is employed. This is a method that has been developed within our group and is currently being evaluated in the clinic for guiding PDT applications, as it provides insights in the pharmacokinetics (through local distribution) of the PS. Thereafter, PDT is applied in this orthotopic tumor model and the efficacy is evaluated *in vivo* by histological analysis. Our data show that nanobody–PS conjugates are selective and able to induce specific tumor cell death in a pre-clinical model of head and neck cancer.

## 2. Materials and methods

### 2.1. Nanobodies and PS conjugation

Nanobodies 7D12, R2, and 7D12-9G8 were produced as described previously, i.e. His-tagged nanobodies were produced in *E. coli* and purified from the periplasmic space by TALON affinity purification [31, 34]. The nanobody 7D12 binds to the domain III of the EGFR, preventing EGF binding to the receptor [39]. The biparatopic nanobody 7D12-9G8 is composed of two nanobodies that bind to different epitopes on EGFR and that cannot bind simultaneously to the same receptor, therefore being able to create clusters of receptors [39]. The irrelevant nanobody R2 is employed as a control and was specifically selected to bind to the azo dye Reactive Red 6 [40,41]. The photosensitizer IRDye700DX (here named PS) was purchased from LI-COR (LI-COR Biosciences, Lincoln, Nebraska) as an N-hydroxysuccinimide (NHS) ester. Conjugation of the PS to the nanobodies was performed as described in Heukers et al. [25], except that the molar ratio for conjugation was 1 to 4 for 7D12–PS and 1 to 2 for R2–PS and 7D12-9G8–PS. After 2 h at room temperature, the conjugates were separated from free PS by size exclusion chromatography using Zebra Spin Desalting columns (Thermo Fisher Scientific, Perbio Science Nederland, Etten-Leur, The Netherlands), in three sequential steps. The degree of conjugation (DOC) was determined as recommended by the provider, by measuring the absorbance at 280 nm and 689 nm using a NanoDrop spectrophotometer (NanoDrop Technologies, Wilmington, Delaware, USA). Purity and integrity of the nanobody–PS conjugates were determined by molecular size separation through SDS-PAGE using 15% gels. Immediately after running the gels, these were imaged on an Odyssey Infrared scanner (LI-COR Biosciences) using the 700 nm channel to detect PS fluorescence. Thereafter, Coomassie Blue staining was performed and detected in the same way as the PS. Cetuximab–PS was used as a reference or positive control in this study and was obtained as described by Mitsunaga et al. [15] for panitumumab.

### 2.2. Cell lines

Three human cell lines with different EGFR expressions were used. The well differentiated squamous cell carcinoma of the tongue OSC-19-luc2-cGFP (high EGFR overexpression) was cultured in Dulbecco's

modified Eagle's medium (DMEM; Invitrogen, Carlsbad, CA) containing 4.5 g D-glucose/L, 110 mg sodium pyruvate/L, 580 mg L-glutamine/L supplemented with 10% fetal bovine serum (FCS; Lonza, Basel, Swiss), 400 IU/mL penicillin, 100 µg/mL streptomycin (Invitrogen) 1 × Minimal Essential Medium (MEM) non-essential amino acids solution and 1 × MEM vitamin solution (Invitrogen) [42]. The human cervical cancer cell line HeLa (intermediate EGFR expression) was cultured in DMEM (Gibco, Invitrogen, United Kingdom) supplemented with 8% FCS (v/v), 100 U/ml penicillin, 100 µg/ml streptomycin, and 2 mM L-glutamine (PAA, Germany) [25]. The human colorectal cancer cell line SW620 (low EGFR) was cultured in Leibovitz's L-15 medium (Invitrogen) containing 300 mg L-threonine/L supplemented with 10% FetalClone II (Hyclone, Logan, UT), 100 IU/mL penicillin, 100 µg/mL streptomycin (Invitrogen) and 20 mM HEPES (Invitrogen) [42]. All cell lines were grown in a humidified incubator at 37 °C and 5% CO<sub>2</sub> and were regularly checked for *Mycoplasma* infection by polymerase chain reaction.

### 2.3. Cell binding assay

A total of 8000 cells were seeded per well of a 96-wells plate (Nunc, Roskilde, Denmark) and allowed to adhere overnight. For the affinity determination, plates were placed at 4 °C and cells were washed with cold binding medium (1% BSA and 25 mM HEPES in DMEM without phenol red, pH 7.2). Subsequently, cells were incubated with a concentration range of nanobody–PS conjugates in binding medium for 2 h at 4 °C. Thereafter, cells were washed twice with cold binding medium and bound conjugates were detected through fluorescence imaging of the PS with the Odyssey Infrared scanner, using the 700 nm channel. Fluorescence intensities were plotted (in triplicate ± SEM) versus the concentrations. The resulting saturation curves were used to determine the apparent affinity ( $K_D$ ) of the nanobody–PS conjugates, using the GraphPad Prism 5.02 software for Windows (GraphPad Software, San Diego, CA), and one-site specific binding, non-linear regression protocol. Experiments were repeated at least twice. For evaluation of the binding specificity by fluorescence microscopy, cells were incubated with 25 nM of nanobody–PS as described above, followed by two washing steps and incubation with calcein AM (0.5 µg/ml, Invitrogen) for detection of cells. This calcein incubation was not performed with OSC cell line as this one is GFP positive and thus already detectable through fluorescence microscopy. Imaging was performed with an EVOS Microscope (Advanced Microscopy Group, AMG, Thermo Fischer Scientific) equipped with 10× objective (Plan Fluor, 10×, NA 0.3, Air and working distance 8.3 mm, AMG) and the following LED-based fluorescence light cubes: GFP (Cat. no. 12-563-470) and Cy5 (for PS detection, Cat. no. 12-563-475) (from Westover Scientific Inc., AMG). Overlays of the separate images were also generated with the EVOS Microscope software (AMG).

### 2.4. Steady-state fluorescence and absorption measurements

The fluorescence quantum yields ( $\Phi_F$ ) of the nanobody/antibody conjugates were determined using a relative method in PBS (pH 7.4) [43] using Chlorin e6 (Ce6) in the same buffer as a reference. At pH 7.4 the fluorescence quantum yield of Ce6 is 0.18 [44,45]. The absorption spectrum of Ce6 and conjugates (concentration  $1 \times 10^{-6}$  M) was recorded in Shimadzu spectrophotometer (UV-2101 PC, Duisburg, Germany). The fluorescence emission of PS was recorded in a Perkin-Elmer spectrofluorometer (LS 50B, Massachusetts, USA). Ce6 and conjugates fluorescence spectra were acquired under 630 nm and 660 nm excitation respectively at an OD lower than 0.1. Calculations of  $\Phi_F$  was accompanied by careful consideration of the differences in photon number at different wavelengths.

### 2.5. Singlet oxygen quantum yield measurements

Photo-oxidation of Singlet Oxygen Sensor Green Reagent (SOSGR) (Molecular Probes, NL) was used to determine the singlet oxygen

formation by the nanobody–PS conjugates. This reagent was used because of its high selectivity for singlet oxygen and low sensitivity to hydroxyl radicals/superoxides [46]. Stock solution of SOSGR (5 mM) was prepared in methanol. The final concentration of SOSGR within the PS solution in PBS pH 7.4 was 1 µM. Solutions of PS and nanobody–PS or antibody–PS conjugates were prepared in PBS pH 7.4. The concentration of PS were adjusted so that all absorb the same number of photons within the irradiated region ( $O.D. = 0.014$  at the  $\lambda_{irr} = 660$  nm (Spectra Physics, NL). Data was acquired in quartz cuvettes in aerobic conditions using stirring under uniform, measured fluence rate at 5 mW/cm<sup>2</sup>. At intervals, the cuvette was removed from magnetic stirrer and absorption and fluorescence emission spectrum ( $\lambda_{exc} = 405$  nm) acquired. The singlet oxygen quantum yields ( $\Phi_D$ ) of conjugates in PBS were determined in duplicate by a relative method [47] with a  $\Phi_D = 0.64$  of Ce6 in the PBS at pH 7.4 as reference [48].

### 2.6. In vitro PDT

One day after seeding 8000 cells per well of 96-wells plates (Greiner Bio-One, Alphen a/d Rijn, The Netherlands), cells are washed once with PDT medium (DMEM without phenol red supplemented with 8% FCS (v/v), 100 U/ml penicillin, 100 µg/ml streptomycin, and 2 mM L-glutamine). Then, a dilution range of nanobody–PS conjugates was added to the cells and incubated for 30 min at 37 °C. After the incubation (also referred to as pulse), cells were washed twice with PDT medium. Immediately after, the fluorescence intensity of the conjugates bound to and/or internalized by the cells was detected with the Odyssey scanner and the cells were illuminated immediately after. Plates were illuminated with ~4 mW/cm<sup>2</sup> fluence rate (measured with an Orion Laser power/energy monitor, Ophir Optronics LTD, Jerusalem, Israel), for a total dose of 10 J/cm<sup>2</sup>, using a device consisting of 96 LED lamps (670 ± 10 nm, 1 LED per well) described in [49,50]. After illumination, cells were placed back into the incubator, unless mentioned otherwise. In all experiments, a number of wells were covered during illumination as internal negative control. Experiments were repeated at least twice.

### 2.7. Cell viability assays

After overnight incubation of the cells treated as described above, cells were incubated with the Alamar Blue reagent, according to the manufacturer's protocol (AbD Serotec, Oxford, United Kingdom), i.e. 10 µl of Alamar Blue was added into each well and mixed with the 100 µl of medium present in the wells. After an incubation of 1 h at 37 °C, fluorescence intensity was measured on a FluoStar Optima fluorescent plate reader (BMG Labtech GmbH, Ortenberg, Germany). Values of fluorescence intensities obtained from wells only containing medium and Alamar blue were taken as background, while wells containing cells that were covered during illumination and that were not treated with nanobody–PS conjugates were set to 100% cell viability. Results are expressed as cell viability in percentage (%), thus relatively to the untreated cells, and the half maximal inhibitory concentration (IC<sub>50</sub>) are determined using the GraphPad Prism 5.02 software.

### 2.8. Co-culture assay

A mixture consisting of 50% of HeLa and 50% of OSC cell lines was seeded in 96-wells plates (Greiner), pulsed with 25 nM of nanobody–PS and followed by 10 J/cm<sup>2</sup> of light dose. After overnight incubation (~16 h), dead cells were distinguished from living cells by propidium iodide (1 µg/ml, Invitrogen) and calcein AM (0.5 µg/ml, Invitrogen) staining, according to the manufacturers' protocol. Cells were imaged with an EVOS Microscope equipped with 10× objective and the following LED-based fluorescence light cubes: GFP for calcein AM and RFP (Cat. no. 12-563-471) for propidium iodide. Phase contrast images were also taken. Overlays of the separate images were generated with the EVOS Microscope software.



## 2.9. Animal model

Nude Balb/c female mice (Charles River laboratories, l'Arbresle, France), aged 4–6 weeks, were housed in individually ventilated cages and provided with food and sterilized water *ad libitum*. Animal experiments were approved by the local animal welfare committee of the Leiden University Medical Center. Orthotopic tongue tumors were submucosally induced in the tip of the tongue through injection of 40,000 OSC-19-luc2-cGFP cells, in suspension in 20  $\mu$ l PBS. General health was monitored twice a week by weight measurements and inspection of the tongue. Tumor growth was monitored twice a week by bioluminescence (BLI) measurements and visual inspection of the tongue. Mice were sacrificed by injection of high-doses ketamine/xylazine.

## 2.10. Quantitative fluorescence spectroscopy

Quantitative fluorescence spectroscopy, which fully corrects for the differences in tissue optical properties, was performed as described previously [51]. White light reflectance and fluorescence spectra were acquired using a single probe that contained two fibers of 0.4 and 0.8 mm. The 0.8 mm fiber was used for both fluorescence and reflectance spectroscopy while the 0.4 mm fiber was used to perform reflectance spectroscopy. The end of the fiber probe in contact with the tissue was polished to an angle of 15° to minimize the collection of specular reflection. To obtain a reflectance spectrum, light from a tungsten halogen lamp was directed on the tissue through a probe containing 2 single fibers with diameters of 0.4 and 0.8 mm. This choice of fiber diameters was dictated by the intention to optically sample a representative proportion of the tumor and normal tissue under interrogation. The photon path length and therefore the sampling volume is on the order of the fiber diameter which means that approximately 1/3 of the tumor volume is interrogated by the smallest fiber diameter. After these sequential reflectance measurements, a single fiber fluorescence spectroscopy (SFF) spectrum was acquired using the 0.8 mm fiber and 660 nm laser light. This wavelength was chosen to optimally separate IRDye700DX (PS) fluorescence from background autofluorescence. The reflectance and fluorescence spectra were detected by three spectrometers, one for each fiber to measure reflectance and one to measure fluorescence where a 675 nm notch filter was used to block scattered excitation light. The spectrometers, light sources and shutters were controlled by a custom made LabView program (National Instruments LabView 7.1) on a notebook computer. A single combined multi-diameter optical fiber (MDSFR)/SFF measurement took approximately 3 s. The fiber probe was removed from the tissue and replaced to perform repeated measurements. Three spectra were acquired from each tissue type, and the average and standard deviation of these measurements were reported.

### 2.10.1. Data analysis

To calculate the intrinsic fluorescence, the raw fluorescence signals were corrected for the effects of absorption and scattering using the optical properties obtained from the MDSFR reflectance spectra. A detailed mathematical description of the recovery of the tissue optical properties from an MDSFR spectrum and their use in determining the intrinsic SFF from a raw fluorescence spectrum has been described previously [52]. The result of this analysis is a calibrated, corrected fluorescence spectrum expressed as the wavelength-dependent intrinsic fluorescence, where  $Q(l)\mu^f$  is the quantum efficiency of the fluorophore at each emission wavelength. This spectrum is then integrated over the emission bandwidth of the fluorophore IRDye700DX (PS) to yield the intrinsic fluorescence  $Q \cdot \mu_{a,x}^f$  where  $Q$  is now the fluorescence quantum yield of the PS.

### 2.10.2. Fluorescence spectral analysis

The fluorescence spectra, corrected for the influence of tissue optical properties, were then analyzed to determine the contribution from the

tissue autofluorescence, and that from PS. A skewed Gaussian was used to fit the autofluorescence while the basis spectra for PS conjugated to each antibody/nanobody were isolated from an average of representative *in-vivo* spectra after subtraction of the autofluorescence [53]. We note that the width and peak of PS fluorescence was slightly different for each antibody/nanobody conjugate.

### 2.10.3. Calibration of the MDSFR/SFF system

Before each set of measurements a careful calibration procedure was performed as described previously [54] consisting of an integrating sphere calibration, a measurement of a calibrated light source, and measurements in water in a dark container and in a liquid phantom containing 1.32% Intralipid with a known reduced scattering coefficient ( $\mu_s'$  at 800 nm = 1.2 mm<sup>-1</sup>). This procedure accounts for variations in the output powers of the light sources and the spectral transmission and sensitivity of the system.

### 2.10.4. Quantitative fluorescence spectroscopy *in vivo*

When OSC tumors were visible by the human eye and the BLI signal ranged between  $5 \times 10^9$  and  $1 \times 10^{10}$  relative light units (RLU), mice were randomly divided into three groups and received an intravenous injection of 200  $\mu$ g of 7D12-PS, 7D12-9G8-PS, or R2-PS, each mouse receiving approximately 6 nmol of PS to allow comparison. Quantitative fluorescence spectroscopy measurements were performed 0.5, 1, 2, 4, 6, 8 and 24 h after injection of the conjugates. Cetuximab-PS was employed as other mAb-PS were described in [15] (i.e. 300  $\mu$ g and also approximately 6 nmol of PS per mouse) and measurements were only performed at 24 h p.i., which corresponded to the selected illumination time point.

## 2.11. Tumor specificity and distribution

Tumor specificity of 7D12-PS and 7D12-9G8-PS was explored by optical imaging *in vivo* and fluorescence imaging of tissue sections. At 1 h after injection of 7D12-PS, 7D12-9G8-PS and R2-PS (200  $\mu$ g), mice were imaged ( $n = 2$ ) with the Pearl imaging system (LI-COR), while kept under isoflurane anesthesia.

In parallel, other mice injected with each of the nanobody-PS conjugates ( $n = 1$ ) had their tongues resected, fixed overnight in 4% formalin and embedded in paraffin blocks. Tissue was sectioned at 10  $\mu$ m and fluorescence imaging was performed using the Odyssey. All images were acquired using the same settings. Further, sections were processed for hematoxylin and eosin (H&E) staining.

## 2.12. Photodynamic therapy

When OSC-19-luc2-cGFP tumors were visible by the human eye and the BLI signal ranged between  $5 \times 10^9$  and  $1 \times 10^{10}$  relative light units (RLU), mice ( $n = 4$  per group) were randomly divided into three groups and received an intravenous injection of 200  $\mu$ g 7D12-PS, 7D12-9G8-PS, R2-PS, or 300  $\mu$ g cetuximab-PS. Based on the quantitative fluorescence spectroscopy measurements, 1 h post-injection (p.i.) was chosen to apply the light. Thus at this time after nanobody-PS administration, or 24 h p.i. of cetuximab-PS injection, mice received painkillers, were put under isoflurane anesthesia, and their tumors were then illuminated using a 690 nm diode laser (Modulight, Tampere, Finland). The power at the end of the optic fiber was calibrated with a power meter (Gigahertz optic, Turkenfeld, Germany). Light was delivered via a 600  $\mu$ m optic fiber with a fluence rate of 50 mW/cm<sup>2</sup> and a homogenous treatment area with the largest diameter of the tumor was used. The exposure time was adjusted to obtain a fluence of 100 J/cm<sup>2</sup>. Mice were sacrificed 24 h after illumination, tongues were collected and frozen on dry ice for subsequent processing for histological analysis of tissue damage.

### 2.13. Histological assessment post-PDT

To assess whether nanobody-targeted PDT is capable of inducing selective tumor cell death *in vivo*, and using antibody-targeted PDT as a positive control, tongues of mice were collected 24 h after application of light for PDT. Thereafter, tongues were sectioned and processed for H&E staining and for CD31 staining of blood vessels. Briefly, for the CD31 staining, sections were subjected to 10 mM tris/EDTA at 96 °C for 20 min. Thereafter, endogene peroxidase was blocked with a solution of 3% hydrogen peroxide. Blocking of aspecific staining was performed with a solution of 5% low fat milk, for 30 min. Then, the primary antibody rabbit anti-CD31 (Abcam, Cambridge, UK) and the secondary antibody goat-anti rabbit biotin (Dako, Heverlee, Belgium) were employed, followed by streptavidin-HRP (Southern Biotech, Birmingham, AL) and the final development of the brown color with DAB, and counterstained with hematoxylin. Pictures were taken with an Olympus microscope equipped with a 4×, 10× or 20× objectives. Two independent researchers scored the damage on H&E tissue sections in percentage (%) of necrosis and scored phototoxicity of normal epithelium, muscle cells, and endothelium (blood vessels), as well as edema, from 0 or 1+ to 3+ by observation of the tumor, and of the blood vessels or the muscle cells, either in close proximity or distant to the tumor. The CD31 staining was employed to score the damage of blood vessels in the tumor area by absence of the brown color. An experienced pathologist was the first observer and was responsible for the training of the second observer. At least 3 sections at different depths were analyzed per tumor. The second observer made use of the Image J software to determine % of necrosis, by drawing regions of necrosis and comparing to the overall region of the tumor. At the end, a consensus was reached on the final score.

### 2.14. Statistical analysis

Data was analyzed using the GraphPad Prism 5.02 software for Windows (GraphPad Software, San Diego, CA). To compare responses to PDT treatment *in vitro*, analysis of significance was performed through unpaired *t*-tests. Intrinsic fluorescence values are reported as mean and standard deviation. Statistical analysis of spectroscopy was performed through a two way ANOVA with the Bonferroni correction. As for the effect *in vivo*, analysis of significance was performed through Mann–Whitney test because of the non-normal distribution of the data. In all cases,  $p < 0.05$  was considered significant.

## 3. Results and discussion

Targeted PDT aims to increase tumor specificity of the PS, in order to enhance the therapeutic effect and spare surrounding normal tissue. In this study, we evaluate the recently introduced nanobody–PS conjugates for their potential to induce specific tumor cell death *in vivo*.

### 3.1. Characterization and EGFR-specific binding of the nanobody–PS conjugates

The nanobodies targeting EGFR used in this study are the monovalent 7D12 [31,33] and the internalizing, biparatopic 7D12–9G8 [34]. In addition, the irrelevant nanobody R2 [40,41] is used as a negative control. These nanobodies were conjugated to the PS (IRDye700DX) via random NHS-mediated coupling to lysine amino acids, similarly to the previous study [25]. After removal of unconjugated PS, SDS-PAGE was used to verify the conjugation. The molecular weights of the fluorescent nanobody–PS conjugates, as detected by fluorescence imaging (top gel, red bands, Fig. 1A), were similar to those of the nanobodies, as demonstrated by the post-Coomassie Blue stained SDS-PAGE gel (bottom gel, black bands, Fig. 1A). Furthermore, very little unconjugated PS was detectable at the front of the gel (Fig. 1A), which rendered the conjugates suitable for both *in vitro* and *in vivo* studies. The PS-to-protein

molar ratios (or degree of conjugation, DOC) of 7D12–PS, 7D12–9G8–PS and R2–PS after random conjugation were on average 0.5, 1.0 and 0.5, respectively. Compared to our previous study, these are different ratios or DOC, except for 7D12–PS. In fact, 0.5 is the highest DOC this nanobody–PS can have while maintaining its low nanomolar binding affinity. For the negative control R2–PS, we chose to use the same DOC as for 7D12–PS (i.e. 0.5, instead of 1.0). To enable the comparison of the therapeutic potential *in vivo*, the DOC of 7D12–9G8–PS was also decreased and used as twice the DOC of 7D12–PS (i.e. 1.0, instead of 1.5). This particular choice was made aiming at the most effective delivery of the drug, i.e. the PS, by the least amount of carrier needed, i.e. protein, in a manner that would allow normalization of PS dose administered *in vivo*. Thus, with the selected DOCs, the *in vivo* administration of equal amounts of protein (i.e. nanobody, in micrograms), result in the administration of equal molar amounts of PS, allowing a better comparison of the therapeutic potential. These two nanobody formats (i.e. 7D12–PS and 7D12–9G8–PS) are two independent carriers used for PS delivery, which are here investigated side-by-side, as it is difficult to anticipate which format is the most promising for *in vivo* application.

Next, the specificity of 7D12–PS and 7D12–9G8–PS for binding to EGFR was demonstrated. For that, besides the human oral squamous cell carcinoma cell line OSC (Fig. 1B), two human control cell lines were employed: the cervical cancer cell line HeLa and the colon cancer cell line SW620 (Fig. 1C). These three cell lines express high, intermediate (or normal), and very low levels of EGFR, respectively. Binding assays were performed at 4 °C to solely explore the binding of conjugates to EGFR. Fluorescence intensities of the bound conjugates correlated well with the level of EGFR expression, i.e. OSC > HeLa > SW620. Moreover, the approximately 2-fold difference in fluorescence intensity observed between the two EGFR targeted nanobody–PS conjugates correlated well with the difference in DOC. Binding affinities of 7D12–PS and 7D12–9G8–PS to high EGFR expressing OSC cells were  $1.9 \pm 0.4$  nM and  $1.0 \pm 0.1$  nM, respectively; and to intermediate EGFR expressing HeLa cells were  $0.7 \pm 0.3$  nM and  $0.5 \pm 0.07$  nM, respectively. Hardly any fluorescence, and thus binding, was observed for 7D12–PS and 7D12–9G8–PS to low EGFR expressing SW620 cells, and for R2–PS and PS to any of the cell lines. To emphasize the specific binding of the nanobody–PS conjugates to EGFR, fluorescence microscopy was performed (Fig. 1D). Among the three cell lines, binding of 7D12–PS and 7D12–9G8–PS was mainly observed in the high EGFR expressing OSC cells (Fig. 1D). As for R2–PS and PS, no fluorescence was observed in any of the three cell lines.

Overall, comparable to our previous study, both 7D12–PS and 7D12–9G8–PS target EGFR specifically. Importantly, this water-soluble PS (IRDye700DX) has no cell binding capacity, unless it is conjugated to the EGFR targeted nanobodies. These facts together could guarantee tumor-specific PDT.

### 3.2. Singlet oxygen quantum yield and *in vitro* efficacy of nanobody–PS conjugates

To determine the relative potency of these nanobody–PS conjugates, singlet oxygen quantum yields ( $\phi_{\Delta}$ ) were measured in test tubes. For that, first, fluorescence quantum yields were determined using a relative method in PBS and Chlorin e6 as a reference. The fluorescence quantum yields of PS, 7D12–PS and 7D12–9G8–PS were  $0.15 \pm 0.03$ ,  $0.14 \pm 0.03$  and  $0.16 \pm 0.03$ , respectively. Interestingly, the determined  $\phi_{\Delta}$  differed significantly between photosensitizer and conjugates: for PS it was determined to be  $0.19 \pm 0.06$ , for 7D12–PS  $0.25 \pm 0.06$ , and for 7D12–9G8–PS  $0.42 \pm 0.07$ . Previous studies have also documented variations in fluorescence and singlet oxygen quantum yields for free PS and conjugates with different DOC [55]. The differences in  $\phi_{\Delta}$ , for the two nanobody–PS conjugates, may be related to variations in amino acids to which the PS is conjugated, thus affecting the environment surrounding PS molecules. Although the efficient generation of singlet oxygen is an important factor in the induction of phototoxic effects,

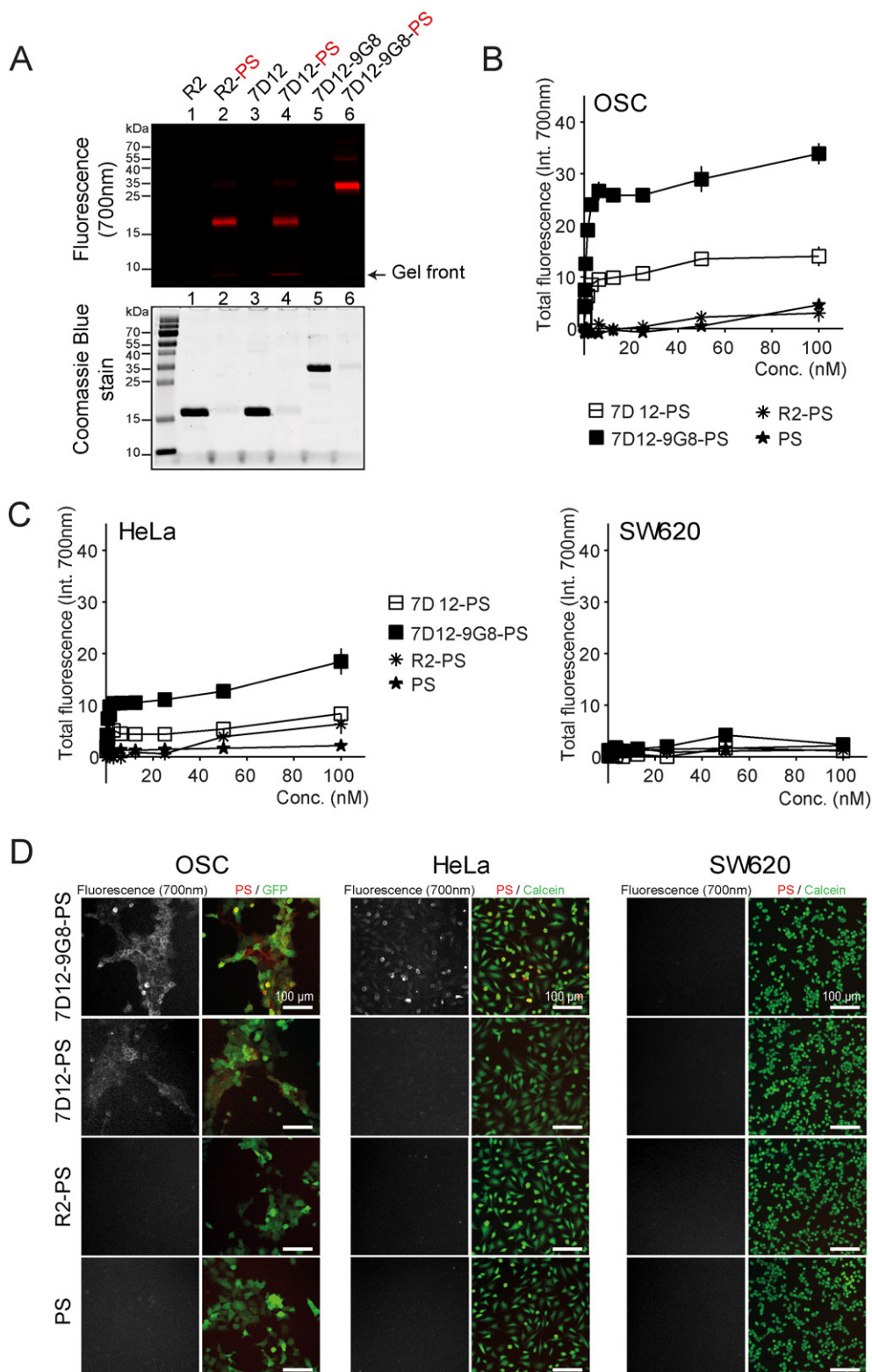


**Fig. 1.** Purity and specificity of nanobody-PS conjugates. (A) Nanobodies and the respective nanobody-PS conjugates are separated by SDS-PAGE, with the following order (numbered 1–6): R2, R2-PS, 7D12, 7D12-PS, 7D12-9G8, and 7D12-9G8-PS. Prior to the Coomassie stain, the fluorescence of the PS is detected (depicted in red, top gel); after the Coomassie stain, the proteins are visualized (depicted in black, bottom gel). (B) Fluorescence intensities of cell bound conjugates are plotted after incubation of OSC cells or (C) the control cell lines HeLa and SW620 with varying concentrations of the EGFR targeted conjugates 7D12-PS and 7D12-9G8-PS, or the controls R2-PS and PS. EGFR expression levels: OSC > HeLa > SW620. (D) Fluorescent microscopy depicting the fluorescence of the nanobody-PS bound to cells (in white, left panels) and that (in red, right panels) overlayed with either GFP (OSC cell line) or calcein staining (HeLa, SW620) for cell visualization (in green, right panels).



the localization of the PS, and variables determining this localization, also influence significantly the overall therapeutic effect.

The phototoxicity of different concentrations of these conjugates was assessed *in vitro* following an incubation time of 30 min. This time period was based on previous work, in which we reported saturable binding of nanobody–PS conjugates after 30 min of incubation [25]. The EGFR targeted nanobody–PS conjugate 7D12-9G8-PS showed to be a very potent PDT agent on OSC cells with an IC<sub>50</sub> value of  $2.2 \pm 0.97$  nM (Fig. 2A). As for 7D12-PS, cell viability was decreased by 32.3% at 50 nM, suggesting an IC<sub>50</sub> higher than 50 nM, though likely below the micromolar range. No reduction of cell viability was observed after illumination of cells incubated with R2-PS or PS alone, indicating the need of specific targeting to induce cell damage (Fig. 2A).

The difference in phototoxicity between 7D12-PS and 7D12-9G8-PS *in vitro* is larger than the difference in fluorescence intensity of the conjugates associated with the cells just before illumination (Supplementary Material, Fig. S1). This could partially be explained by the higher singlet oxygen quantum yield of 7D12-9G8-PS. Furthermore, several studies pointed to an intracellular localization of the PS as important to increase the phototoxicity of mAbs-PS [56–58]. In fact, as we showed in our previous study, more 7D12-9G8-PS is delivered intracellularly compared to 7D12-PS, which has been described to be via clustering induced endocytosis of EGFR [25]. Thus, both aspects are likely to explain the higher potency of 7D12-9G8-PS *in vitro*. Our previous study showed even lower IC<sub>50</sub> values for 7D12-PS and 7D12-9G8-PS, though that can

be partly justified by a lower DOC for 7D12-9G8-PS in the current study, and also by the different EGFR expression levels of the cell lines employed. In our previous study, A431 and 14C cell lines were employed which have higher EGFR expression than the OSC cells.

Here, to confirm that the phototoxicity is indeed dependent on the EGFR level, toxicity was also assessed on cell lines with different EGFR expression levels (Fig. 2B, i.e. HeLa and SW620), and indeed the phototoxicity was lower than the values obtained with OSC cells, which related to the extent of conjugate bound to cells (Supplementary Material, Fig. S1), and correlated to the EGFR expression as demonstrated in Fig. 1B and C. The IC<sub>50</sub> on HeLa cells was  $33.5 \pm 1.4$  nM for 7D12-9G8-PS, while 7D12-PS induced almost no effect in the concentration range here tested (i.e. highest concentration 50 nM). These are significantly lower toxicities than observed in high EGFR expressing OSC cells. No IC<sub>50</sub> could be calculated for SW620 cells indicating the absence of cell damage on low EGFR expressing cells (Fig. 2B).

Co-culture experiments were performed to assess the selectivity of these nanobody–PS conjugates toward OSC cells overexpressing EGFR, among intermediate EGFR expressing HeLa cells (Fig. 2C). In these co-cultures, HeLa and OSC cells could be distinguished by the differences in morphology and GFP fluorescence imaging of cGFP transfected OSC cells (i.e. OSC-19-luc2-cGFP). 7D12-PS and 7D12-9G8-PS induced phototoxicity only to OSC cells, as indicated by the propidium iodide staining (indicative of dead cells, Fig. 2C) that coincides with GFP fluorescence. Also here, 7D12-9G8-PS showed to be more toxic than

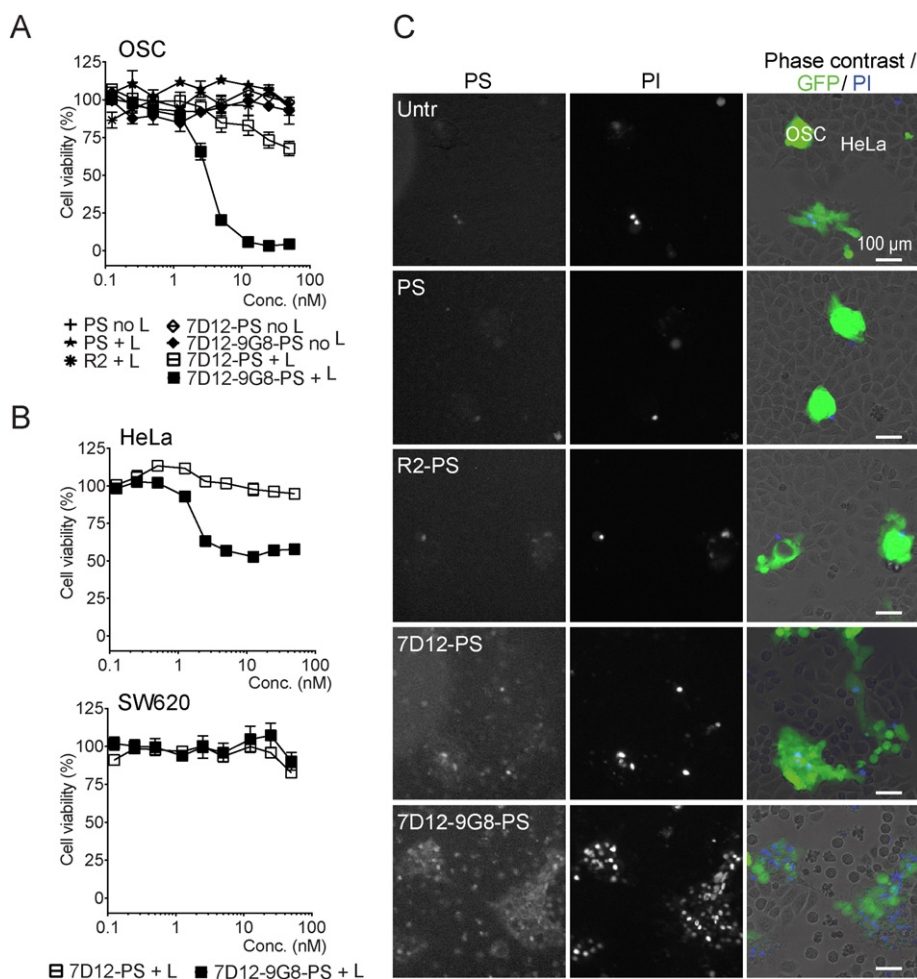


**Fig. 2.** Nanobody–PS are phototoxic to EGFR overexpressing cells. Phototoxicity of nanobody–PS conjugates and controls in (A) OSC, (B) HeLa and SW620 cells presented as percentage (%) of cell viability after a  $10 \text{ J/cm}^2$  light dose. Data depicted as means  $\pm$  SEM. (C) Fluorescence and phase contrast images of co-cultures of HeLa and OSC cells after PDT with nanobody–PS conjugates or the controls R2–PS and PS. Left panel depicts PS fluorescence, middle panel propidium iodide (PI) to identify dead cells, and right panel the overlay of PI with both GFP and phase contrast to visualize cells. Cells can be differentiated by morphology and fluorescence of the GFP (green) positive OSC cells.

7D12–PS, as illustrated by the higher number of dead cells. No PS nor phototoxicity was observed under the same conditions on HeLa cells (See Supplementary Material for similar treatment on these two cell lines separately, Fig. S2).

### 3.3. Pharmacokinetics and macroscopic localization of nanobody–PS conjugates

To investigate the selectivity and potency of these nanobody–PS conjugates in a pre-clinical model of head and neck cancer, the OSC cell line was inoculated and grown orthotopically in tongues of nude mice. Being the first pre-clinical study, we have decided to use a reference for validation of the procedure here employed: we used Cetuximab–PS as Mitsunaga et al. [15] have described the use of their mAb–PS conjugates, i.e. with a DOC of 3.0 and injecting a dose of 300  $\mu\text{g}$  per mouse, which are equivalent to approximately 6 nmol of PS. With these particular conditions, we expected to induce tumor cell death and subsequently validate the procedure selected for analysis. Based on the selected DOC of the different nanobody–PS, the dose of protein to be injected was calculated so that it was normalized for the amount of drug carried, i.e. PS.

For an effective PDT without damage to normal tissue, light should be applied locally at the most favorable time point post-injection (p.i.) of the nanobody–PS conjugates. This is when the highest dose of PS is located at the tumor, and the lowest dose in the surrounding tissues. In practice, this generally corresponds to a balance between the dose of PS at the tumor and a sufficient tumor-to-background ratio (TBR). As the nanobody–PS conjugates are traceable through optical imaging, wide field fluorescence imaging gives insights into their tumor specificity and distribution *in vivo*. However, the differences in optical properties of different tissues greatly influence the number of collected fluorescent photons. Alternatively, determining the intrinsic fluorescence enables a quantitative comparison of fluorescence's pharmacokinetics locally in tissues with different and/or varying optical properties (such as in tumor, normal tongue, and skin). Our group has been investigating the use of empirical modeling and point reflectance spectroscopy with multi-diameter optical fibers (MDSFR) combined with single fiber fluorescence spectroscopy (SFF) to measure the tissue optical properties  $\mu_a$ ,  $\mu'_s$ , and thereby recovering the intrinsic fluorescence from the interrogated volume [52]. This approach is particularly important when the optical properties of tumor and normal tissue are known to be significantly different [51]. Using this method, the quantitative fluorescence pharmacokinetics were assessed for the PS (IRDye700DX) in each conjugate. The intrinsic fluorescence reported in this study, defined as  $Q^f\mu'_a$ , is the product of the fluorescence quantum yield of the PS and its absorption coefficient at 660 nm. While reliable estimates of  $Q^f$  and the *in vivo* extinction spectrum of the PS would allow for the quantitative determination of its concentration *in vivo*, we considered it sufficient for this study to determine the intrinsic fluorescence.

No significant differences were observed in normal tongue tissue between all conjugates. At all time points, significantly less R2–PS was present in the tumor compared to 7D12–PS and 7D12–9G8–PS ( $p < 0.05$  for all time point) (Fig. 3A). For 7D12–PS, more conjugate was present in the tumor compared to that in normal tongue tissue and skin, proving tumor specificity *in vivo*. Differences were statistically significant ( $p < 0.05$ ) at time-point 0.5, 1, 6 and 24 h p.i. The maximum amount of 7D12–PS in the tumor was observed already at 30 min p.i., after which it slowly decreased, correlating with our previous imaging study [31], and possibly related to the unbinding of non-internalized conjugates. However, a relatively high value of fluorescence was also present in normal tongue tissue at 30 min p.i. At 1 h p.i. the fluorescence at the normal tongue tissue decreased slightly and a TBR of  $1.8 \pm 0.3$  was obtained. Although at a later time point the TBR increased, such as to a value of  $16.1 \pm 4.5$  at 24 h p.i. (Fig. 3B), the total fluorescence of 7D12–PS in the tumor at 24 h p.i. had already decreased 42% from the intrinsic fluorescence at 1 h p.i. Differences in TBR of 7D12–PS, compared to R2–PS, were statistically significant at 24 h p.i. ( $p < 0.0001$ ).

Similar results were obtained for 7D12–9G8–PS, showing tumor specificity *in vivo* as significantly more conjugate was present in the tumor compared to that in normal tongue tissue and skin ( $p < 0.05$  for all time points, except for 8 h p.i.). Unlike 7D12–PS, the highest intrinsic fluorescence at the tumor was observed for a longer period, i.e. during the first 4 h p.i., which is possibly related to a more pronounced internalization and less unbinding of non-internalized conjugate. Already at 1 h p.i. a TBR of  $3.8 \pm 0.5$  was obtained. Also in this case, higher TBR could be obtained at later time points, such as  $30.8 \pm 0.9$  at 24 h p.i. The differences in TBR of 7D12–9G8–PS, compared to R2–PS, were statistically significantly at both 1 and 24 h p.i. ( $p = 0.0024$  and  $p < 0.0001$ , respectively). However 24 h p.i. the intrinsic fluorescence had also in this case decreased 39%, compared to 1 h after the injection.

One could expect that high TBRs are needed to spare normal tissue, and to enable accurate tumor detection with fluorescence imaging (in the setting of image-guided PDT). Nevertheless, in principle, the actual amount of PS in the tissue predominantly determines the actual photo-toxic effect. Therefore, in order to maximize the concentration of PS while retaining a suitable TBR, we decided to subsequently apply the light locally at the tumor 1 h p.i. of the nanobody–PS conjugates.

Clear differences were observed on the values of intrinsic fluorescence of the two EGFR targeted nanobody–PS conjugates, where higher values were obtained for 7D12–9G8–PS in the tumor at all times, compared to 7D12–PS. Thus, 7D12–9G8–PS seems to be the best nanobody format to carry PS to the tumor. Although additional experiments are needed to further clarify these differences, at this point we can speculate that these could be related to the different nanobody formats, i.e. monovalent versus biparatopic, and their different distribution and binding in tumors. In fact, the enhanced internalization documented for 7D12–9G8 *in vitro* [25] could play an important role. We have observed more internalization of 7D12–9G8–PS than 7D12–PS, after 30 min incubation *in vitro*, thus at 1 h after i.v. injection it is well possible that the same trend can affect the results observed *in vivo*. In addition, differences are to some extent related to the different DOC of the nanobody–PS, as this was 0.5 for 7D12–PS and 1.0 for 7D12–9G8–PS. Although, the equal dose of protein given (in micrograms) allowed the injection of equal amounts of PS molecules per mouse, approximately half of the 7D12 molecules were conjugated to PS, whereas all molecules of 7D12–9G8 injected contained a PS. As a consequence, competition of conjugated 7D12–PS and unconjugated 7D12 for binding to the EGFR, could have contributed to the lower intrinsic fluorescence and TBRs of 7D12–PS, compared to 7D12–9G8–PS.

In order to further elucidate the mechanism(s) underlying the efficacy of our conjugates compared to that of a mAb–PS conjugate, we also performed quantitative spectroscopy in animals 24 h after the injection of cetuximab–PS (which was the time point employed in previous studies for mAb–PSs [15], with DOC of 3.0, equivalent PS injected as the other mice). At this time point the average value of  $Q^f\mu'_a$  was  $0.0374 \pm 0.0045$ ,  $0.0057 \pm 0.0019$  and  $0.0036 \pm 0.0007$ , in tumor, normal tongue, and in skin, respectively, with a corresponding TBR of  $6.5 \pm 0.9$ . These tumor values for  $Q^f\mu'_a$  are significantly greater ( $\sim 7.5$ -fold) than the maximum fluorescence intensity early after the injection of 7D12–9G8–PS and the TBR exceeds the TBR found for 7D12–9G8–PS at 1 h p.i. Despite the same dose of PS had been injected with this mAb–PS as with the nanobody–PS conjugates, these results suggest that the mAb–PS is the most effective carrier for higher accumulation of PS at the tumor. This is likely a consequence of a combination of the longer half-life of cetuximab–PS in the blood stream, which leads to later accumulation of the conjugate at the tumor (i.e. 24 h instead of 1 h p.i.), and the higher DOC of cetuximab–PS. It is important to note that quantitative spectroscopy provides a volume average signal (over  $\sim 1 \text{ mm}^3$ ) and does not retain any information on the microscopic distribution of the conjugates. Therefore, additional studies are required to compare the microscopic localization of the different conjugates.

To further validate the 1 h p.i. as being the optimal time point for illumination, a number of mice ( $n = 2$ ) were subjected to *in vivo* optical



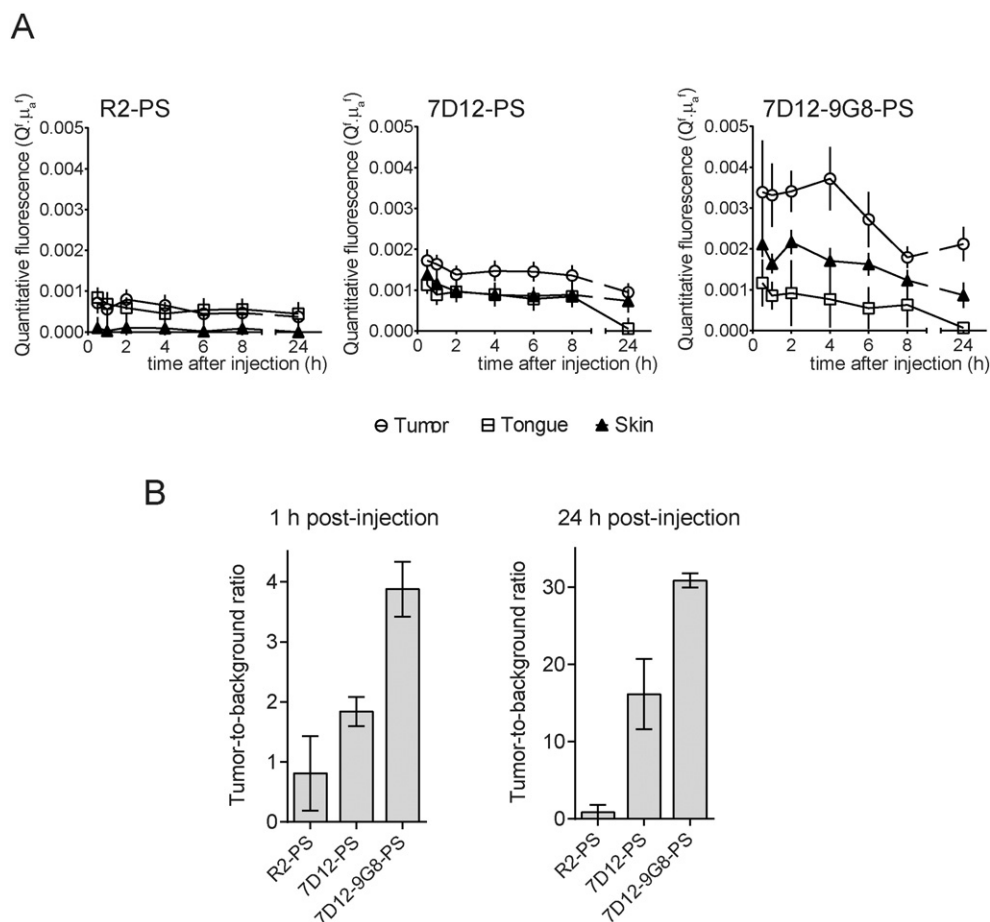


**Fig. 3.** Quantitative fluorescence spectroscopy for selecting the illumination time point. (A) Local assessment of the intrinsic fluorescence of the nanobody-PS conjugates at the tumor, normal tongue and skin, as an indication of their pharmacokinetics. Intrinsic fluorescence,  $Q \cdot \mu_a$ , is the product of the fluorescence quantum yield of the PS and its absorption coefficient at 660 nm. Average values of  $Q \cdot \mu_a$  are calculated from 0 to 24 h after injection of nanobody-PS conjugates. (B) Tumor-to-background ratio (TBR) at 1 h and 24 h p.i. of the different nanobody-PS conjugates, calculated from intrinsic fluorescence measurements. Error bars represent the standard deviation of the calculated TBRs.

imaging at that time point after injection of the different nanobody-PS conjugates. Clearly, very little fluorescence is observed at the tongue when R2-PS was injected, in contrast to the highly fluorescent tongues shown when mice were injected with either 7D12-PS or 7D12-9G8-PS (Fig. 4A). These images support the specificity documented earlier (Fig. 3). In parallel, tongues of mice were collected 1 h p.i. of the nanobody-PS conjugates and were processed for fluorescence imaging and histology. These analyses confirmed that both EGFR targeted conjugates are tumor specific. Already at 1 h p.i. of 7D12-PS and 7D12-9G8-PS, a clear colocalization of fluorescence and tumor could be observed, confirming tumor specificity (Fig. 4B). No tumor accumulation was observed in sections of tongues of mice injected with the control R2-PS. Importantly, nanobody-PS conjugates showed a homogeneous distribution through the solid tumor, which is in agreement with our previous optical imaging study [31] and is expected to contribute to treatment efficacy.

#### 3.4. In vivo evaluation of nanobody-targeted PDT

Besides the best time point for illumination (i.e. 1 h p.i.), an important consideration for optimizing the efficacy of the nanobody-PS conjugates *in vivo* is the choice of PDT illumination parameters: fluence and fluence rate. The latter was chosen to be 50 mW/cm<sup>2</sup> to avoid any heating of the illuminated tissue and to maximize the ability of the tumor vasculature to supply oxygen during illumination. The former parameter, the therapeutic light fluence (or dose) was chosen to be 100 J/cm<sup>2</sup> in order to maximize PDT efficacy, considering the penetration of the laser light (690 nm, which is the excitation maximum for

this PS) in the tongue and the inevitable photobleaching of the PS during the illumination. It is important to note that this light fluence may be reduced, in the future, after a full optimization of the illumination parameters has been performed. Given the difficulty of light fluence (rate) treatment planning in mice, we chose to accept the potential over-treatment of the underlying normal tissue in the present study.

Thus, 1 h p.i. of the nanobody-PS conjugates, illumination was performed superficially on the tongue of mice. As positive control for *in vivo* PDT, we injected mice with cetuximab-PS, which were then illuminated 24 h p.i., similar to the study of Mitsunaga et al. [15]. Thereafter, to determine whether the conjugates were capable of inducing selective tumor cell death *in vivo*, mice were sacrificed at 24 h post-PDT and their tongues were processed for histological analyses. All the controls, i.e. light only and R2-PS, 7D12-PS and 7D12-9G8-PS without application of light, presented a viable and dense tumor (H&E), as well as numerous blood vessels (CD31 staining), indicating that neither light alone, nor the nanobody-PS conjugates without light were capable of inducing damage (Fig. 5A). The antibody-targeted PDT led to tumor damage, which validates the model and procedure here employed, although with a broad variation of degree of necrosis, ranging from 25 to 70% (median 57.5%, Fig. 5A, B). Numerous blood vessels remained intact after this PDT, as observed in the corresponding CD31 staining. An unexpected mild to moderate tumor damage was obtained with R2-PS (median 42.5%, range 20–50% necrosis, Fig. 5B), likely a bystander effect due to vascular damage, as suggested by the heavily coagulated blood vessels observed just below the tip of the tongue and the absence of CD31 staining in the tumor area, though viable tumor is still observed (Fig. 5A, Table 1). Whether R2-PS is specifically associating with

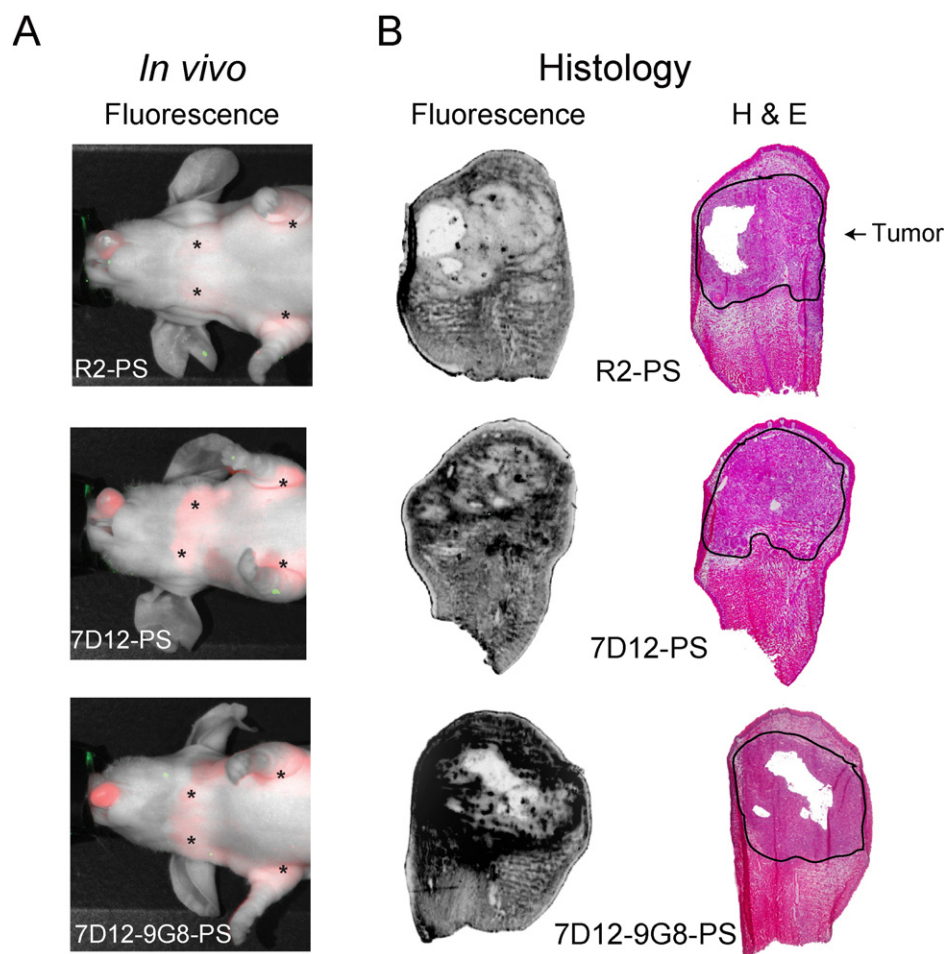


**Fig. 4.** EGFR-targeted nanobody-PS conjugates specifically localize in tumors. (A) Optical imaging of mice 1 h p.i. of the nanobody-PS conjugates. Images were obtained with a Pearl imaging system. Brightness of individual illustrations is manually adjusted to highlight the location of the fluorescence. Asterisks (\*) indicate lymph nodes. (B) Fluorescence imaging of the PS (in dark) and H&E staining of sections of tongues obtained from mice 1 h p.i. of the nanobody-PS conjugates. OSC tumors are distinguished at the higher half of the tongues, by a characteristic dense mass of tumor cells, delimited by a dark line.

endothelial cells is not clear at this point in time, though this may be an explanation for these observations. On the contrary, for both nanobody formats targeting EGFR, a more homogenous damage to the tumor is observed, reaching even 90% of necrosis (Fig. 5A, B). In the case of 7D12-PS, a very localized and reproducible damage was induced at the tumor site (median 80%, range 80–90% necrosis), with minimal effect on the CD31 staining of blood vessels around the tumor (brown color present), whereas inside the tumor no CD31 staining was observed (Fig. 5A, Table 1). With 7D12-9G8-PS, some variation between mice was observed in the extent of damage induced (median 80%, range 60–90% necrosis), and slightly more coagulation was observed at the blood vessels surrounding the tumor (compared to 7D12-PS) (Fig. 5A, Table 1). Notably, the two EGFR targeted nanobody-photosensitizer conjugates were the only format of conjugates capable of inducing 90% necrosis (Fig. 5B). 7D12-PS induced significantly more necrosis compared to both R2-PS ( $p = 0.0256$ ) and cetuximab-PS ( $p = 0.0265$ ) (Fig. 5B). Due to the variation in effect induced in mice with 7D12-9G8-PS, the extent of necrosis was significantly higher compared to R2-PS ( $p = 0.0284$ ), but not compared to cetuximab-PS ( $p = 0.1102$ ) (Fig. 5B).

Interestingly, although spectroscopy experiments showed a significantly higher concentration of cetuximab-PS at the time point of irradiation compared to 7D12-9G8-PS and 7D12-PS, significantly more necrosis was observed with the nanobody-PS conjugates. In fact, these *in vivo* results suggest that the most effective and reproducible treatment was obtained with the monovalent 7D12-PS conjugate. Importantly, we realize that at this point conclusions should be very

carefully drawn as these are in fact three different antibody formats and thus three independent carrier systems for PS, here investigated side-by-side in very particular conditions. Nevertheless, these results are remarkable, in light of the observations obtained with quantitative fluorescence spectroscopy revealing a lower concentration of PS and lower TBR obtained with the 7D12-PS conjugate, compared to 7D12-9G8-PS or cetuximab-PS. Furthermore, while 7D12-9G8-PS was more toxic than 7D12-PS *in vitro* (Fig. 2), also in respect of induction of necrosis (Supplementary Material, Fig. S3), *in vivo* efficacy studies point to a higher phototoxicity induced by 7D12-PS. This increase in efficacy of the monovalent 7D12-PS could be due to its small size, which likely enables better penetration into the interior of tumors and a more homogenous distribution. It is well accepted that the diffusion of molecules from the blood vessels and their subsequent penetration through tissues is influenced by factors such as molecular weight, size, charge, affinity, and antigen expression among others [59,60]. Furthermore, using small nanobodies, the PS is in closer proximity to the cell membrane which could increase phototoxicity. More studies are certainly needed to better understand the differences observed in PDT efficacy between 7D12-PS and 7D12-9G8-PS *in vivo*, and future studies will also demonstrate whether the significant differences in necrosis will result in differences in survival. However, at this point, it is clearly suggested that the overall amount of PS accumulated in the tumor is not *per se* the limiting factor for efficacy, but the way it is distributed is likely very critical. The more homogenous and reproducible degree of damage induced by 7D12-PS, as compared to cetuximab-PS, is in agreement with our former study showing differences in intratumoral distribution



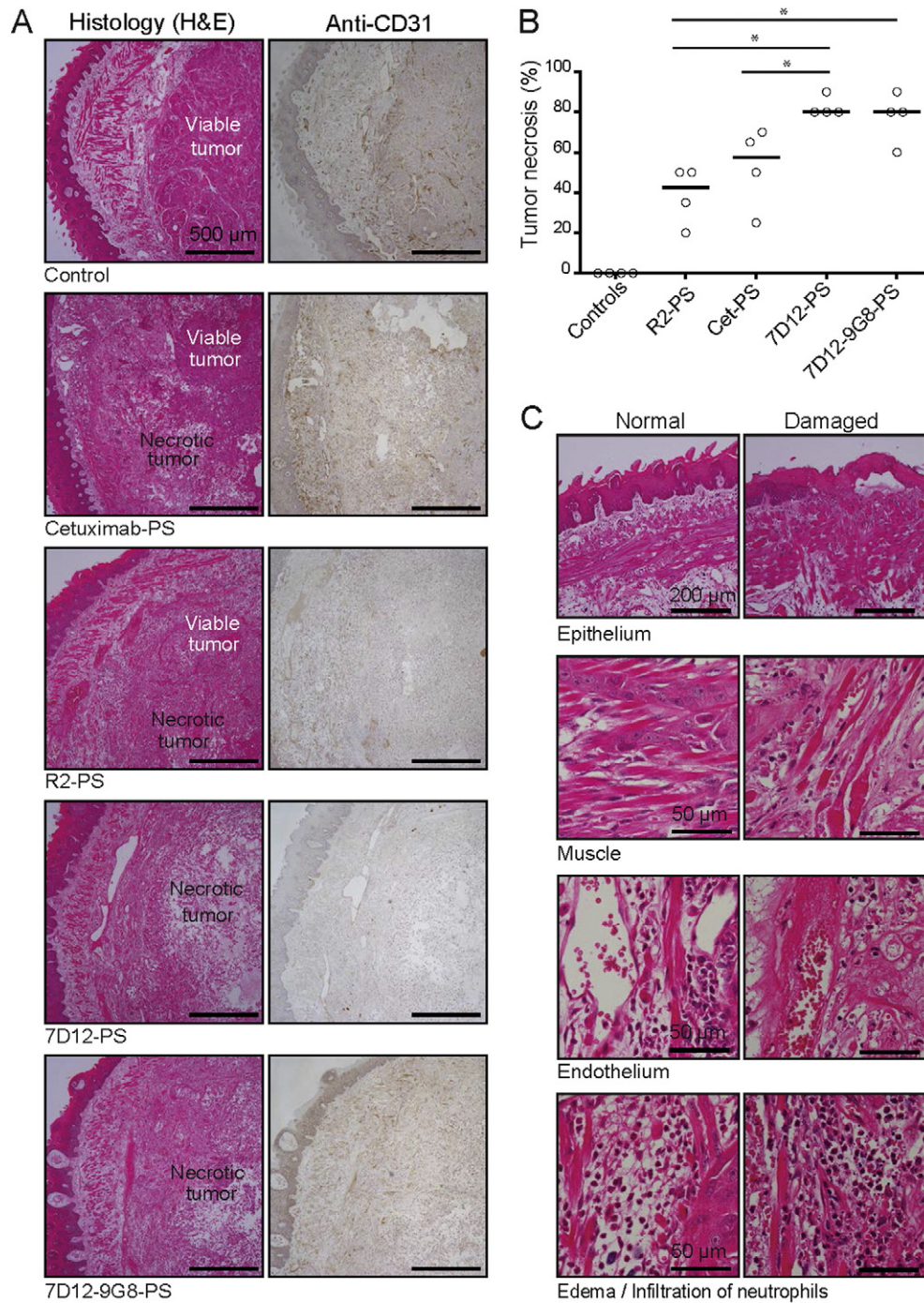


**Fig. 5.** *In vivo* tumor specific phototoxicity of nanobody-PS conjugates. (A) Sections of tongues of mice collected 24 h post-PDT, processed for histology (H&E) and anti-CD31 staining to assess phototoxicity of the different treatments: intravenous administration of R2-PS, 7D12-PS or 7D12-9G8-PS followed by illumination 1 h p.i., or cetuximab-PS followed by illumination 24 h p.i. These are compared to the controls: light alone or each nanobody-PS conjugate without illumination. Each image is representative of the results obtained for that group. Areas of viable or necrotic tumor are indicated and blood vessels are highlighted by the anti-CD31 staining (in brown). (B) Percentages (%) of tumor necrosis obtained for each single treatment are depicted together with the median value. (C) Representative examples of damage to the epithelium, muscle cells, endothelium, and of edema and infiltration of neutrophils indicating recruitment of immune cells.

of 7D12 and cetuximab in A431 xenografts [31]. In a similar context, Watanabe et al. [24] have recently compared a mAb-PS (150 kDa) with a minibody-PS (80 kDa) and a diabody-PS (50 kDa), where the PS was IRDye700DX, and found that the use of the smallest fragment (in this case a diabody) resulted in the shortest time interval between injection and light exposure without compromising therapeutic efficacy. These results differ from ours, in that we found a difference in phototoxicity with our nanobody-PS conjugates (15 or 30 kDa), to the advantage of the smaller nanobody-PS conjugates compared to the

antibody-PS conjugate. The disparity between these results could be explained by the differences in format and/or size of diabody-PS and nanobody-PS conjugates.

Besides the extent of damaged tumor, damage to the epithelium and other features were also scored (Table 1, with examples given in Fig. 5C). Overall, no significant damage to the epithelium was induced by any of the treatments, other than the damage likely associated with handling of the tongues with a pincette. Damage to muscle cells was common to all treatments on the cells nearest to the tumor, but absent



**Table 1**

Several features are scored to characterize the damage observed in Fig. 5.

	Controls	R2-PS	Cet-PS	7D12-PS	7D12-9G8-PS
Edema	+	++	++	++	++/+++
Presence of mast cells	+	+ / ++	+	+	+
Presence of neutrophils	—	+ / ++	+++	++	+ / ++
Damage to muscle cells					
Around the tumor	—	+	+	+ / ++	+
Away from tumor	—	—	—	—	—
Damage to epithelium	—	5–10%	5–10%	5–10%	5%
Damage to blood vessels (H&E)					
Around the tumor	—	++	+	+ / ++	++
Away from tumor	—	—	—	—	—
Absence of CD31 stain					
Inside the tumor	—	++ / +++	++ / +++	+++	++ / +++
Around the tumor	—	+	+	+	+
Away from the tumor	—	—	—	—	—
Remarks	—	Coagulation	—	—	—

in muscle cells away from the tumor. Blood vessel damage varied for the different groups, although the trend was a more pronounced damaged in the tumor or in blood vessels surrounding the tumor and no damage further away from the tumor. Due to necrosis, the damage to muscle cells and blood vessels inside the tumor was not possible to score accurately from H&E sections. Edema was always present, while the extent of infiltration of neutrophils or mast cells varied, suggesting that PDT mediated by this PS (IRDye700DX) is also capable of recruiting immune cells. Future studies will have to prove how these inflammatory responses affect overall treatment efficacy.

Vascular targeted PDT is very dependent on the time interval between PS administration and illumination. Here, we have selected 1 h p.i. for the nanobody-PS conjugates and 24 h p.i. for cetuximab-PS, to promote tumor targeted PDT. Shorter intervals could possibly lead to more vascular damage, also risking damage to normal tissues. Clearly, the time point selected was appropriate for 7D12-PS and 7D12-9G8-PS as this resulted in minimal damage of blood vessels and normal muscle cells around the tumor and no damage of blood vessel and normal muscle cells away from the tumor area. These details also indicate that high TBRs are not a requirement, in this particular form of PDT, to damage the tumor and spare normal tissue (TBRs obtained were  $1.8 \pm 0.3$  for 7D12-PS and  $3.8 \pm 0.5$  for 7D12-9G8-PS). This is an interesting observation that could have important implications for the PDT field. Possibly, it is an effect of this particular PS, as this PS does not lead to any damage unless it is conjugated to a targeting molecule (nanobody) that binds to cells. Furthermore, the observation of minimal damage around the tumor also suggests appropriate selection of the fluence for the illumination. In fact, as much as the laser was pointed to the tumor, normal tissue surrounding it was certainly also exposed to the illumination to some extent. Additionally, the light only control (Fig. 5A) also proved that the selected parameters are safe for normal tissues. Further *in vivo* research focused on varying nanobody-PS conjugate dose, illumination time point, and fluences for shorter treatment times, could optimize this protocol further. In such protocol optimization, quantitative fluorescence spectroscopy may be of substantial benefit, allowing patient- and tumor-specific planning for illuminations.

The considerable efforts made in the field to render PDT tumor specific [14,61–63] have recently resulted in first-in-human trials, such as NCT02422979 ([clinicaltrials.gov](http://clinicaltrials.gov)), which is testing an antibody-PS conjugate composed of cetuximab and IRDye700DX. This trial will certainly have an impact in the field and hopefully stimulate additional trials that will encourage the use of targeted PDT as a standard treatment in the clinic. Even though antibody-targeted PDT has now entered a clinical trial, as demonstrated in this study, nanobody-targeted PDT has the potential to even further improve clinical PDT: through rapid accumulation and fast clearance of the conjugates, enabling light application very shortly after conjugate administration and minimizing possible photosensitivity. These would likely bring benefits in respect of hospital management and costs involved per treatment. In fact, nanobody-

targeted PDT has great potential to be translated to the clinic. First, because the PS investigated here is already being employed in a clinical trial, and second, because nanobodies have been in clinical trials for several years in areas other than oncology (e.g. antithrombotic nanobody [64]). The possibility for clinical translation surely should encourage additional research to further explore this approach of nanobody-targeted PDT.

#### 4. Conclusions

Overall, the EGFR targeted nanobody-PS conjugates 7D12-PS and 7D12-9G8-PS are selective and potent PDT agents that specifically accumulate in tumors *in vivo*. Upon local illumination within 1 h after administration, these conjugates lead to pronounced tumor necrosis and to the infiltration of immune cells. This study highlights the therapeutic potential of these novel nanomedicines and stimulates further research, contributing to the exploration of nanobody-targeted PDT.

#### Acknowledgements

This work was performed with the financial support of the STW-NWO VENI grant number 11878 and by the European Commission through a H2020-MSCA-RISE-2014 award under grant number 644373.

#### Appendix A. Supplementary data

Supplementary data to this article can be found online at <http://dx.doi.org/10.1016/j.jconrel.2016.03.014>.

#### References

- [1] I.A.F.R.O.C.W.H. Organisation, Globocan 2012: Estimated Cancer Incidence, Mortality and Prevalence Worldwide in 2012, 2012.
- [2] L.A. Torre, F. Bray, R.L. Siegel, J. Ferlay, J. Lortet-Tieulent, A. Jemal, Global cancer statistics, 2012, *CA Cancer J. Clin.* 65 (2015) 87–108.
- [3] P. Agostinis, K. Berg, K.A. Cengel, T.H. Foster, A.W. Girotti, S.O. Gollnick, S.M. Hahn, M.R. Hamblin, A. Juzeniene, D. Kessel, M. Korbelik, J. Moan, P. Mroz, D. Nowis, J. Piette, B.C. Wilson, J. Golab, Photodynamic therapy of cancer: an update, *CA Cancer J. Clin.* 61 (2011) 250–281.
- [4] B. Green, A.R. Cobb, C. Hopper, Photodynamic therapy in the management of lesions of the head and neck, *Br. J. Oral Maxillofac. Surg.* 51 (2013) 283–287.
- [5] B. Karakullukcu, H.J. Nyst, R.L. van Veen, F.J. Hoebers, O. Hamming-Vrieze, M.J. Witjes, S.A. de Visscher, F.R. Burlage, P.C. Levendag, H.J. Sterenborg, I.B. Tan, mTHPC mediated interstitial photodynamic therapy of recurrent nonmetastatic base of tongue cancers: development of a new method, *Head Neck* 34 (2012) 1597–1606.
- [6] A.E. O'Connor, W.M. Gallagher, A.T. Byrne, Porphyrin and nonporphyrin photosensitizers in oncology: preclinical and clinical advances in photodynamic therapy, *Photochem. Photobiol.* 85 (2009) 1053–1074.
- [7] R.R. Allison, G.H. Downie, R. Cuenca, X.H. Hu, C.J. Childs, C.H. Sibata, Photosensitizers in clinical PDT, *Photodiagn. Photodyn. Ther.* 1 (2004) 27–42.
- [8] R.R. Allison, C.H. Sibata, Oncologic photodynamic therapy photosensitizers: a clinical review, *Photodiagn. Photodyn. Ther.* 7 (2010) 61–75.
- [9] C.J. Gomer, Preclinical examination of first and second generation photosensitizers used in photodynamic therapy, *Photochem. Photobiol.* 54 (1991) 1093–1107.

- [10] A.S. Derycke, P.A. de Witte, Liposomes for photodynamic therapy, *Adv. Drug Deliv. Rev.* 56 (2004) 17–30.
- [11] G.A. van Dongen, G.W. Visser, M.B. Vrouenraets, Photosensitizer–antibody conjugates for detection and therapy of cancer, *Adv. Drug Deliv. Rev.* 56 (2004) 31–52.
- [12] S.A. Sibani, P.A. McCarron, A.D. Woolfson, R.F. Donnelly, Photosensitizer delivery for photodynamic therapy. Part 2: systemic carrier platforms, *Expert Opin. Drug Deliv.* 5 (2008) 1241–1254.
- [13] W.M. Sharman, J.E. van Lier, C.M. Allen, Targeted photodynamic therapy via receptor mediated delivery systems, *Adv. Drug Deliv. Rev.* 56 (2004) 53–76.
- [14] N.S. Soukos, M.R. Hamblin, S. Keel, R.L. Fabian, T.F. Deutsch, T. Hasan, Epidermal growth factor receptor-targeted immunophotodiagnosis and photoimmunotherapy of oral precancer in vivo, *Cancer Res.* 61 (2001) 4490–4496.
- [15] M. Mitsunaga, M. Ogawa, N. Kosaka, L.T. Rosenblum, P.L. Choyke, H. Kobayashi, Cancer cell-selective in vivo near infrared photoimmunotherapy targeting specific membrane molecules, *Nat. Med.* 17 (2011) 1685–1691.
- [16] R.A. Beckman, L.M. Weiner, M. Davis, Antibody constructs in cancer therapy: protein engineering strategies to improve exposure in solid tumors, *Cancer* 109 (2007) 170–179.
- [17] G.M. Thurber, S.C. Zajic, K.D. Wittrup, Theoretic criteria for antibody penetration into solid tumors and micrometastases, *J. Nucl. Med.* 48 (2007) 995–999.
- [18] I. Bronshteint, S. Aulova, A. Juzeniene, V. Iani, L.W. Ma, K.M. Smith, Z. Malik, J. Moan, B. Ehrenberg, In vitro and in vivo photosensitization by protoporphyrins possessing different lipophilicities and vertical localization in the membrane, *Photochem. Photobiol.* 82 (2006) 1319–1325.
- [19] L.R. Duska, M.R. Hamblin, M.P. Bamberg, T. Hasan, Biodistribution of charged F(ab')<sub>2</sub> photoimmunoconjugates in a xenograft model of ovarian cancer, *Br. J. Cancer* 75 (1997) 837–844.
- [20] M.K. Kuimova, M. Bhatti, M. Deonarain, G. Yahsioglu, J.A. Levitt, I. Stamati, K. Suhling, D. Phillips, Fluorescence characterisation of multiply-loaded anti-HER2 single chain Fv-photosensitizer conjugates suitable for photodynamic therapy, *Photochem. Photobiol. Sci.* 6 (2007) 933–939.
- [21] C. Staneloudi, K.A. Smith, R. Hudson, N. Malatesti, H. Savoie, R.W. Boyle, J. Greenman, Development and characterization of novel photosensitizer: scFv conjugates for use in photodynamic therapy of cancer, *Immunology* 120 (2007) 512–517.
- [22] M. Bhatti, G. Yahsioglu, L.R. Milgrom, M. Garcia-Maya, K.A. Chester, M.P. Deonarain, Targeted photodynamic therapy with multiply-loaded recombinant antibody fragments, *Int. J. Cancer* 122 (2008) 1155–1163.
- [23] L.R. Milgrom, Towards recombinant antibody-fragment targeted photodynamic therapy, *Sci. Prog.* 91 (2008) 241–263.
- [24] R. Watanabe, H. Hanaoka, K. Sato, T. Nagaya, T. Harada, M. Mitsunaga, I. Kim, C.H. Paik, A.M. Wu, P.L. Choyke, H. Kobayashi, Photoimmunotherapy targeting prostate-specific membrane antigen: are antibody fragments as effective as antibodies? *J. Nucl. Med.* 56 (2015) 140–144.
- [25] R. Heukers, P.M. van Bergen En Henegouwen, S. Oliveira, Nanobody-photosensitizer conjugates for targeted photodynamic therapy, *Nanomed.: Nanotechnol., Biol. Med.* 10 (2014) 1441–1451.
- [26] C. Hamers-Casterman, T. Atarhouch, S. Muyldermans, G. Robinson, C. Hamers, E.B. Songa, N. Bendahman, R. Hamers, Naturally occurring antibodies devoid of light chains, *Nature* 363 (1993) 446–448.
- [27] S. Oliveira, R. Heukers, J. Sornkom, R.J. Kok, P.M. van Bergen En Henegouwen, Targeting tumors with nanobodies for cancer imaging and therapy, *J. Control. Release* 172 (2013) 607–617.
- [28] S. Muyldermans, Nanobodies: natural single-domain antibodies, *Annu. Rev. Biochem.* 82 (2013) 775–797.
- [29] S. Muyldermans, T. Atarhouch, J. Saldanha, J.A. Barbosa, R. Hamers, Sequence and structure of VH domain from naturally occurring camel heavy chain immunoglobulins lacking light chains, *Protein Eng.* 7 (1994) 1129–1135.
- [30] M. Kijanka, F.J. Warders, M. El Khatatbi, M. Lub-de Hooge, G.M. van Dam, V. Ntziachristos, L. de Vries, S. Oliveira, P.M. van Bergen En Henegouwen, Rapid optical imaging of human breast tumour xenografts using anti-HER2 VHHs site-directly conjugated to IRDye 800CW for image-guided surgery, *Eur. J. Nucl. Med. Mol. Imaging* 40 (2013) 1718–1729.
- [31] S. Oliveira, G.A. van Dongen, M. Stigter-van Walsum, R.C. Roovers, J.C. Stam, W. Mali, P.J. van Diest, H.M. van Bergen En Henegouwen, Rapid visualization of human tumor xenografts through optical imaging with a near-infrared fluorescent anti-epidermal growth factor receptor nanobody, *Mol. Imaging* 11 (2012) 33–46.
- [32] M.M. Schmidt, K.D. Wittrup, A modeling analysis of the effects of molecular size and binding affinity on tumor targeting, *Mol. Cancer Ther.* 8 (2009) 2861–2871.
- [33] L.O. Gainkam, L. Huang, V. Cavaliere, M. Keyaerts, S. Hernot, I. Vaneycken, C. Vanhove, H. Revets, P. De Baetselier, T. Lahoutte, Comparison of the biodistribution and tumor targeting of two 99mTc-labeled anti-EGFR nanobodies in mice, using pinhole SPECT/micro-CT, *J. Nucl. Med.* 49 (2008) 788–795.
- [34] R.C. Roovers, M.J. Vosjan, T. Laeremans, R. el Khoulati, R.C. de Bruin, K.M. Ferguson, A.J. Verkleij, G.A. van Dongen, P.M. van Bergen En Henegouwen, A biparatopic anti-EGFR nanobody efficiently inhibits solid tumour growth, *J. Int. Cancer* 129 (2011) 2013–2024.
- [35] J.R. Grandis, D.J. Tweardy, Elevated levels of transforming growth factor alpha and epidermal growth factor receptor messenger RNA are early markers of carcinogenesis in head and neck cancer, *Cancer Res.* 53 (1993) 3579–3584.
- [36] K.K. Ang, B.A. Berkey, X. Tu, H.Z. Zhang, R. Katz, E.H. Hammond, K.K. Fu, L. Milas, Impact of epidermal growth factor receptor expression on survival and pattern of relapse in patients with advanced head and neck carcinoma, *Cancer Res.* 62 (2002) 7350–7356.
- [37] X. Peng, D.R. Draney, W.M. Volcheck, G.R. Bashford, D.T. Lamb, D.L. Grone, Y. Zhang, C.M. Johnson, Phthalocyanine dye as an extremely photostable and highly fluorescent near-infrared labeling reagent, 2006 (pp. 60970E–60970E–60912).
- [38] R. Heukers, J.F. Vermeulen, F. Ferreidouni, A.N. Bader, J. Voortman, R.C. Roovers, H.C. Gerritsen, P.M. van Bergen En Henegouwen, Endocytosis of EGFR requires its kinase activity and N-terminal transmembrane dimerization motif, *J. Cell Sci.* 126 (2013) 4900–4912.
- [39] K.R. Schmitz, A. Bagchi, R.C. Roovers, P.M. van Bergen En Henegouwen, K.M. Ferguson, Structural evaluation of EGFR inhibition mechanisms for nanobodies/VHH domains, *Structure* 21 (2013) 1214–1224.
- [40] L.G. Frenken, R.H. van der Linden, P.W. Hermans, J.W. Bos, R.C. Ruuls, B. de Geus, C.T. Verrips, Isolation of antigen specific llama VHH antibody fragments and their high level secretion by *Saccharomyces cerevisiae*, *J. Biotechnol.* 78 (2000) 11–21.
- [41] E. Dolk, C. van Vliet, J.M. Perez, G. Vriend, H. Darbon, G. Ferrat, C. Cambillau, L.G. Frenken, T. Verrips, Induced refolding of a temperature denatured llama heavy-chain antibody fragment by its antigen, *Proteins* 59 (2005) 555–564.
- [42] P.B. van Driel, J.R. van der Vorst, F.P. Verbeek, S. Oliveira, T.J. Snoeks, S. Keereweere, B. Chan, M.C. Boonstra, J.V. Frangioni, P.M. van Bergen En Henegouwen, A.L. Vahrmeijer, C.W. Lowik, Intraoperative fluorescence delineation of head and neck cancer with a fluorescent anti-epidermal growth factor receptor nanobody, *Int. J. Cancer* 134 (2014) 2663–2673.
- [43] J. Lakowicz, Principles of Fluorescence Spectroscopy, third ed. Springer, New York, 2006.
- [44] E. Zenkevich, E. Sagun, V. Knyukshto, A. Shulga, A. Mironov, O. Efremova, R. Bonnett, S.P. Songca, M. Kassem, Photophysical and photochemical properties of potential porphyrin and chlorine photosensitizers for PDT, *J. Photochem. Photobiol. B Biol.* 33 (1996) 171–180.
- [45] M.V. Parkhots, V.N. Knyukshto, G.A. Isakov, P.T. Petrov, S.V. Lepeshkevich, A. Ya, Khairullina, B.A. Dzhagarov, Spectral-luminescent studies of the “Photolon” photosensitizer in model media and in mol. of cancer, *J. Appl. Spectrosc.* 70 (2003) 921–926.
- [46] Invitrogen, Molecular Probes Product Information, 2004.
- [47] F.W. Wilkinson, W.P. Helman, A.B. Ross, Quantum yields for the photosensitized formation of the lowest electronically excited singlet state of molecular oxygen in solution, *J. Phys. Chem.* 22 (1993) 113–262.
- [48] R.W. Redmond, J.N. Gamlin, A compilation of singlet oxygen yields from biologically relevant molecules, *Photochem. Photobiol.* 70 (1999) 391–475.
- [49] C.J. Rijcken, J.W. Hofman, F. van Zeeland, W.E. Hennink, C.F. van Nostrum, Photosensitizer-loaded biodegradable polymeric micelles: preparation, characterization and in vitro PDT efficacy, *J. Control. Release* 124 (2007) 144–153.
- [50] J.W. Hofman, M.G. Carstens, F. van Zeeland, C. Helwig, F.M. Flesch, W.E. Hennink, C.F. van Nostrum, Photocytotoxicity of mTHPC (temoporfin) loaded polymeric micelles mediated by lipase catalyzed degradation, *Pharm. Res.* 25 (2008) 2065–2073.
- [51] F. van Leeuwen-van Zaane, U.A. Gamm, P.B. van Driel, T.J. Snoeks, H.S. de Bruijn, A. van der Ploeg-van den Heuvel, I.M. Mol, C.W. Lowik, H.J. Sterenberg, A. Amelink, D.J. Robinson, In vivo quantification of the scattering properties of tissue using multi-diameter single fiber reflectance spectroscopy, *Biomed. Opt. Expr.* 4 (2013) 696–708.
- [52] F. van Leeuwen-van Zaane, U.A. Gamm, P.B. van Driel, T.J. Snoeks, H.S. de Bruijn, A. van der Ploeg-van den Heuvel, H.J. Sterenberg, C.W. Lowik, A. Amelink, D.J. Robinson, Intrinsic photosensitizer fluorescence measured using multi-diameter single-fiber spectroscopy in vivo, *J. Biomed. Opt.* 19 (2014) 15010.
- [53] S. Brooks, C.L. Hoy, A. Amelink, D.J. Robinson, T.E. Nijsten, Sources of variability in the quantification of tissue optical properties by multi-diameter single-fiber reflectance and fluorescence spectroscopy, *J. Biomed. Opt.* 20 (2015) 57002.
- [54] C.L. Hoy, U.A. Gamm, H.J. Sterenberg, D.J. Robinson, A. Amelink, Method for rapid multi-diameter single-fiber reflectance and fluorescence spectroscopy through a fiber bundle, *J. Biomed. Opt.* 18 (2013) 107005.
- [55] S.L. Rakestraw, W.E. Ford, R.G. Tompkins, M.A. Rodgers, W.P. Thorpe, M.L. Yarmush, Antibody-targeted photolysis: in vitro immunological, photophysical, and cytotoxic properties of monoclonal antibody-dextran-Sn(IV) chlorin e6 immunoconjugates, *Biotechnol. Prog.* 8 (1992) 30–39.
- [56] D. Mew, C.K. Wat, G.H. Towers, J.G. Levy, Photoimmunotherapy: treatment of animal tumors with tumor-specific monoclonal antibody-hematoporphyrin conjugates, *J. Immunol.* 130 (1983) 1473–1477.
- [57] M. Carcenac, M. Dorvillius, V. Garambois, F. Glaussel, C. Larroque, R. Langlois, N.E. Hynes, J.E. van Lier, A. Pelegri, Internalisation enhances photo-induced cytotoxicity of monoclonal antibody-phthalocyanine conjugates, *Br. J. Cancer* 85 (2001) 1787–1793.
- [58] M.B. Vrouenraets, G.W. Visser, F.A. Stewart, M. Stigter, H. Oppelaar, P.E. Postmus, G.B. Snow, G.A. van Dongen, Development of meta-tetrahydroxyphenylchlorin-monomer antibody conjugates for photoimmunotherapy, *Cancer Res.* 59 (1999) 1505–1513.
- [59] A.I. Minchinton, I.F. Tannock, Drug penetration in solid tumours, *Nat. Rev. Cancer* 6 (2006) 583–592.
- [60] M.E. Ackerman, D. Pawlowski, K.D. Wittrup, Effect of antigen turnover rate and expression level on antibody penetration into tumor spheroids, *Mol. Cancer Ther.* 7 (2008) 2233–2240.
- [61] M.D. Savellano, T. Hasan, Targeting cells that overexpress the epidermal growth factor receptor with polyethylene glycolated BPD verteporfin photosensitizer immunoconjugates, *Photochem. Photobiol.* 77 (2003) 431–439.
- [62] M.D. Savellano, T. Hasan, Photochemical targeting of epidermal growth factor receptor: a mechanistic study, *Clin. Cancer Res.* 11 (2005) 1658–1668.
- [63] A.O. Abu-Yousif, A.C. Moor, X. Zheng, M.D. Savellano, W. Yu, P.K. Selbo, T. Hasan, Epidermal growth factor receptor-targeted photosensitizer selectively inhibits EGFR signaling and induces targeted phototoxicity in ovarian cancer cells, *Cancer Lett.* 321 (2012) 120–127.
- [64] O. Muller, J. Bartunek, M. Hamilos, C.T. Berza, F. Mangiacapra, A. Ntalianis, K. Vercruysse, C. Duby, W. Wijns, B. De Bruyne, G.R. Heyndrickx, M. Vanderheyden, J.B. Holz, E. Barbato, von Willebrand factor inhibition improves endothelial function in patients with stable angina, *J. Cardiovasc. Transl. Res.* 6 (2013) 364–370.